



# Using micro focus industrial computed tomography to characterize the effects of soil type and soil depth on soil pore characteristics, morphology, and soil compression in Xi'an, China

Kun Yu<sup>1</sup> · Yang Duan<sup>2</sup> · Maosheng Zhang<sup>3</sup> · Ying Dong<sup>3</sup> · Luchen Wang<sup>1</sup> · Ye Wang<sup>1</sup> · Xu Guo<sup>1</sup> · Fusheng Hu<sup>1</sup>

Received: 17 March 2019 / Accepted: 29 November 2019 / Published online: 19 December 2019  
© Springer-Verlag GmbH Germany, part of Springer Nature 2019

## Abstract

**Purpose** Land subsidence has caused serious geological damage in many countries, including China. Soil pore number, size, shape, and pore size distribution affect soil deformation and thus land subsidence. Quantification of complex pore structures in different soil types and at various soil depths, however, remains cumbersome. The objective of this study was to quantify pore characteristics of three different soil types using computed tomography (CT) technique, investigate the effects of soil depth, examine the relationships between various parameters, and preliminarily determine the pore deformation pattern.

**Materials and methods** Undisturbed soil samples (70 mm diameter × 50 mm height) of clay, silt, and silty clay soils were collected from two 300-m-deep engineering geological boreholes on both sides of the Xi'an D7 ground fissure. One hundred CT images were acquired for each soil sample. Soil pore characteristics and morphological parameters, including porosity, macroporosity, coarse mesoporosity, microporosity, number of pores, number of macropores (diameter > 1000 μm), number of coarse mesopores (diameter 200–1000 μm), number of micropores (diameter < 200 μm), circularity, structure model index, degree of anisotropy, and the Euler number, were analyzed.

**Results and discussion** Micropores were generally regularly shaped and the main contributors to the total number of pores, whereas macropores were mostly elongated and contributed to total porosity. With increasing depth, the most noticeable changes appeared in silt soil and the least noticeable in clay soil. The alternate pore deformation pattern was significant in silt and silty clay soils.

**Conclusions** Soil depth significantly influenced all soil pore parameters, whereas soil type significantly affected the remaining parameters, except circularity and degree of anisotropy. The elongated macropores in silt and silty clay soils favor land subsidence in the Xi'an area. The present results can help optimize the groundwater exploitation layer, reducing soil compaction and land subsidence in this area.

**Keywords** Image analysis · Micro-computed tomography · Pore characteristics · Pore deformation · Pore morphology · Soil compaction

---

Responsible editor: Fanghua Hao

**Electronic supplementary material** The online version of this article (<https://doi.org/10.1007/s11368-019-02536-8>) contains supplementary material, which is available to authorized users.

✉ Yang Duan  
duanyang@caep.org.cn

<sup>1</sup> School of Water Resources and Environment, China University of Geosciences (Beijing), Beijing 100083, China

<sup>2</sup> State Environmental Protection Key Laboratory of Environmental Planning and Policy Simulation, Chinese Academy of Environmental Planning, Beijing 100012, China

<sup>3</sup> Xi'an Center of Geological Survey, China Geological Survey, Beijing 100012, China

## 1 Introduction

As an environmental geological phenomenon, land subsidence is a worldwide problem (Xu et al. 2008; Shen et al. 2015; Wang et al. 2016) that causes not only great damage to public infrastructure (Du et al. 2012; Bian et al. 2016) but also a number of geo-hazards and serious economic loss (Li et al. 2000; Yin et al. 2005). The total area of subsidence amounts to 93,885 km<sup>2</sup> in China (Cui 2008). In the 1990s, annual land subsidence reached a maximum value of about 130 mm/year in Xi'an (Wang et al. 2019). Although land subsidence can result from many factors, the primary one is excessive extraction of groundwater (Xue et al. 2005).

Dissipation of pore water pressure and compaction of the soil skeleton are key factors in soil deformation (Terzaghi 1943). Therefore, soil pores play an important role in land subsidence.

Previous studies showed that soil type, land use, tillage, and compaction were among the main factors influencing pore characteristics and thereby affecting the chemical, physical, and biological processes in the soil (Gantzer and Anderson 2002; Cameira et al. 2003; Bhattacharyya et al. 2006; Lipiec et al. 2006, 2012; Zhou et al. 2008; Udawatta et al. 2008; Mooney and Morris 2008; Cássaro et al. 2011; da Costa et al. 2014; Feng et al. 2018; Hu et al. 2018b). Luo et al. (2010) found that soil type, land use, and their interaction significantly affected macroporosity, network density, surface area, length density, node density, and mean angle. Pore morphology and pore size distribution (PSD) have been shown to markedly influence the compressibility of soils (Griffiths and Joshi 1991; Hong et al. 2006; Low et al. 2008). Moreover, another important factor in soil deformation is thickness of the soil layer (Wu et al. 2008). Critically, even within the same soil type, soil pore characteristics and morphology will vary with depth (stress). At present, the relationship between soil type, soil depth, and soil structure is ambiguous. Therefore, visualization and quantification of soil pore characteristics and morphology represent an effective way to better understand and predict soil compaction.

X-ray computed tomography (CT) was first developed in the early 1970s for medical imaging. In recent years, it has attracted growing attention by researchers in soil and earth sciences because conventional methods often fail to provide detailed information about pore characteristics or spatial distribution (Gantzer and Anderson 2002; Meng et al. 2017) and, sometimes, porosity is estimated by indirect procedures (Beven and Germann 1982). The advantage of X-ray CT, especially micro focus industrial CT, is a finer resolution on a millimeter- to micrometer-scale, the ability to precisely map the position of pores, the possibility of quantitative image analysis, and the nondestructive nature of the technique (Gantzer and Anderson 2002; Mooney 2002; Carlson et al. 2003; Pöhlitz et al. 2018). For example, Udawatta et al. (2006) have used X-ray CT to evaluate and compare the effects of different buffers on pore parameters. Schäffer et al. (2007) successfully analyzed the deformation of macropore structures under mechanical loads using quantitative morphometry of X-ray micro-CT images. Moreover, Kim et al. (2010) used CT scanning images to evaluate the effect of compaction on geometry and related parameters of macropores in soil. Hu et al. (2018a) used CT to evaluate the effect of shrub roots on soil macropores. All these studies indicate that X-ray CT could be suitable for quantifying soil pore characteristics.

Land subsidence has caused a number of geo-hazards and substantial economic losses in recent years in Xi'an, including ground fissures and damage to pipelines or other underground

infrastructure (Bian et al. 2017; Cheng et al. 2017a, b, 2018a, b; Shen et al. 2017; Lai et al. 2017, 2018; Qiu et al. 2017, 2018; Wang et al. 2018). It is closely related to soil deformation and seepage of groundwater, both of which are linked to soil pore characteristics. It should be noted that previous studies on land subsidence such as numerical models were conducted mostly from a macroscopic perspective, and parameters such as porosity were considered as constants. With the application of CT technology, discussion about the relationships between pore characteristics, morphology, and land subsidence from the microscopic perspective is possible. Therefore, the objectives of this study were to (1) quantify soil pore characteristics and morphology using X-ray micro-CT and image analysis for three different soil types in Xi'an; (2) evaluate the influence of soil type and soil depth on the CT-measured pore parameters; and (3) describe how pore characteristics affect soil compaction in this area. Determining a link between soil deformation and microstructural changes will help estimate land subsidence potential, optimize numerical model parameters, and adjust pumping depth to reduce land subsidence.

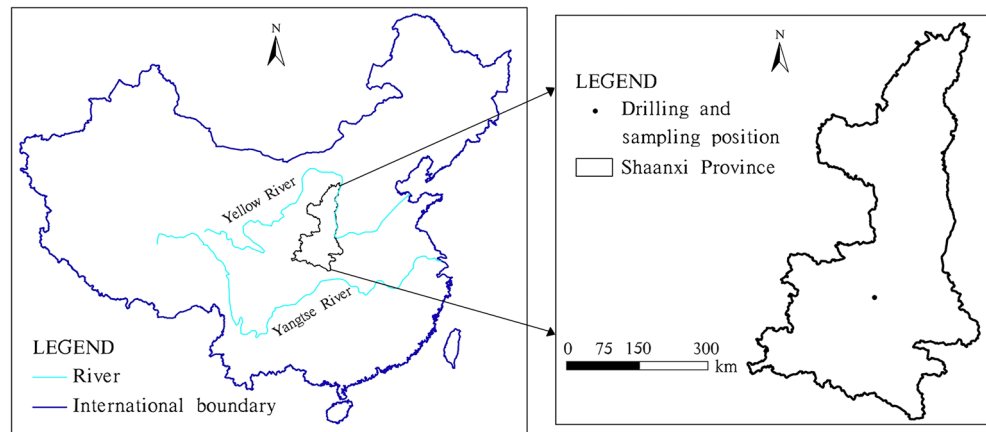
## 2 Materials and methods

### 2.1 Study sites, soil sampling, and preparation

The samples for the study were collected from two engineering geological boreholes on the north and south sides of the D7 ground fissure in Xi'an (Fig. 1 and Table S1 - Electronic Supplementary Material). The complex aquifer-aquitard system consists of intercalated sands, clays, silts, and silty clays, which make the precise delineation of the strata rather difficult. Fig. S1 (ESM) illustrates geomedia stratification and the aquifer division in YHG-1 and YHG-2 boreholes. There are three aquitards and three confined aquifers within boreholes, and the water level in the area is about 53 m underground. According to Gambolati and Freeze (1973); Gambolati et al. (1974), the main compacted soil for land subsidence is clayey soil, so we selected clay, silt, and silty clay soils at corresponding depths in different aquifers and aquitards. The sampled depths of different soil types are presented in Table 1 and Fig. S1 (ESM). Twenty-one undisturbed soil samples were collected using cylindrical stainless-steel samplers with a diameter of 7.0 cm and a length of 5.0 cm (Zhao et al. 2017b). The soil cylinders were placed in plastic bags, sealed, labeled, placed in an aluminum sample container with cushioning material, and transferred to the laboratory. The soil samples were stored in a refrigerator at 4 °C until experiments were conducted.

To avoid the shielding and reflection effect of the metal container during X-ray scanning, and to cope with the limited size of the CT sample stage, the samples were cut using

**Fig. 1** Map showing the location of the study area in China and the sampling site in Shaanxi Province



Plexiglas rings with a diameter of 5.0 cm, length of 2.0 cm, and a 2.0-mm-thick wall. The Plexiglas ring was evenly applied with Vaseline on the inside and then pressed into the soil samples. Excess soil at the top and bottom was removed, and soil samples were placed in water for saturation to maintain the soil structure (Rabbi et al. 2016; Reichert et al. 2016).

Soil samples were continuously dripped with non-air water for 2 h and then placed in a vacuum-saturated tank for 24 h to ensure that they were completely saturated (>98%). To mimic the state of natural ground stress and scan at a strain-locked state, a unique compression device was constructed (Fig. 2). The device had to be small enough to fit into the micro-CT system and to be penetrable by X-rays. Considering the difference of soil density and material density, acrylic glass was used for the construction of the device except for pressure rods (Schäffer et al. 2008). The compression process did not consider horizontal deformation, and the pressure under the contact area of the pressure sensor was converted by stress. The self-weight stress was obtained by the following equation (Powrie 2014):

$$\sigma_v = \gamma z \quad (1)$$

where  $\sigma_v$  is the self-weight stress of soil,  $\gamma$  is the unit weight of soil, and  $z$  is the thickness of the overlying soil layer. For samples above the water level, the average  $\gamma$  in this region was 18 kN/m<sup>3</sup>; for samples below the water level, the effective  $\gamma$  was 10 kN/m<sup>3</sup>. Compression was applied evenly, vertically and diagonally (60°), while the soil sample was being adequately drained. Soil sample displacement was recorded by a displacement gauge, which was fixed with a cross bar. The soil sample was considered to be stable if the deformation was less than 1 mm after 2 h. Then, the sample was placed in the CT scanner along with the device.

## 2.2 CT scanning and image processing

A Nikon XTH 320LC CT scanner at the Micro Focus Industrial CT Laboratory, China University of Geosciences (Beijing), was used to scan the soil samples.

The scan system parameters were set to 100 kV, power of 18.6 W, 960 mm focal length of scanning, and 3  $\mu$ m voxel resolution to provide detailed and low-noise projections. The X-ray beam width was 0.015 mm, which produced a volume element (voxel) size of 0.018 mm<sup>3</sup>. Each soil sample was positioned horizontally on the scanning stage so that the X-ray intersected it perpendicularly to its longitudinal axis. A total of 21 soil samples were scanned and 2100 images were analyzed (100 images per soil sample). The data were then stored for following image analysis.

The images were processed, visualized, and quantified using the public domain software ImageJ version 1.51i. A rectangular region of 72.71 mm<sup>2</sup> (7.88 mm  $\times$  9.23 mm) was demarcated by the *Area Selection Tools* as the “region of interest (ROI)” to exclude the effect of voids near the sample walls and to minimize beam hardening interference; the exterior region was deleted using *Clear Outside Tools*. The circular artifact was removed by polar coordinate transformation after cutting the image. To differentiate pores and soil solids, 8-bit grayscale images were converted into binary images using the *Threshold Tool*. Specifically, 76 (range is 0 to 255) was chosen as the threshold value, following selection using the modified IsoData algorithm and the method mentioned in Hu et al. (2016). In the images, the black areas were considered to be pores and the white areas indicated soil solids (Fig. 3).

Number of pores, porosity, and PSD were obtained using *Analyze Particles Tool*. Pore perimeter was used to estimate the pore diameter, and the pores were classified into three classes based on their diameter: macropores (>1000  $\mu$ m), coarse mesopores (200–1000  $\mu$ m), and micropores (<200  $\mu$ m) according to Kim et al. (2010). The pore area of an image was divided by the 72.71 mm<sup>2</sup> total area to estimate porosity as well as macroporosity, coarse mesoporosity, and microporosity. A detailed description of image analysis can be found in Udawatta et al. (2006).

**Table 1** CT-measured number of pores (pores, macropores, coarse mesopores, and micropores) and porosity (porosity, macroporosity, coarse mesoporosity, and microporosity) as influenced by clay, silt, and silty clay soil types and depth ( $n = 21$ )

	Depth (m)	Number	Porosity (%)						
			Pores	Macropores	Coarse mesopores	Micropores			
Soil type means									
Clay		3571 ± 367 a	46 ± 20 a	247 ± 87 a	3278 ± 394 a	41.80 ± 2.95 b	26.80 ± 5.63 b	8.00 ± 3.08 a	7.00 ± 1.00 a
Silt		2630 ± 625 b	38 ± 10 b	181 ± 51 b	2410 ± 591 b	48.50 ± 5.04 a	37.25 ± 7.63 a	6.13 ± 1.72 b	5.38 ± 1.30 b
Silty clay		3102 ± 960 ab	32 ± 12 c	175 ± 58 b	2895 ± 927 ab	44.50 ± 3.74 ab	33.00 ± 6.23 ab	5.75 ± 1.91 b	5.75 ± 1.04 ab
Depth means									
Clay	17.32	3731 ± 283 b	70 ± 7 a	352 ± 32 a	3309 ± 257 c	42.76 ± 1.93 b	24.24 ± 3.30 c	10.74 ± 1.00 a	7.78 ± 0.67 a
	23.05	3625 ± 238 c	21 ± 3 e	146 ± 17 e	3458 ± 232 b	46.47 ± 2.68 a	35.78 ± 2.81 a	4.31 ± 0.48 d	6.38 ± 0.46 c
	73.42	3988 ± 464 a	40 ± 7 c	263 ± 36 c	3684 ± 434 a	41.66 ± 4.41 c	25.77 ± 6.20 b	8.01 ± 1.15 b	7.87 ± 0.88 a
	98.20	2994 ± 223 e	63 ± 6 b	302 ± 34 b	2629 ± 205 d	38.86 ± 1.95 d	21.39 ± 3.33 d	10.89 ± 1.15 a	6.58 ± 0.56 b
	170.78	3517 ± 453 d	34 ± 6 d	172 ± 23 d	3310 ± 438 c	39.29 ± 5.73 d	26.96 ± 6.85 b	6.07 ± 0.90 c	6.26 ± 0.75 c
Silt	37.45	2663 ± 299 d	22 ± 6 g	117 ± 24 f	2525 ± 276 d	53.48 ± 4.98 b	44.97 ± 6.24 b	3.86 ± 0.90 f	4.66 ± 0.58 d
	68.25	2118 ± 270 e	35 ± 8 e	154 ± 27 e	1928 ± 244 e	56.71 ± 4.74 a	47.64 ± 5.83 a	4.85 ± 0.90 e	4.22 ± 0.55 e
	111.12	1643 ± 369 f	29 ± 13 f	103 ± 41 g	1512 ± 320 f	52.28 ± 6.86 b	45.97 ± 8.52 b	3.76 ± 1.41 f	3.05 ± 0.83 f
	150.50	2691 ± 384 d	38 ± 8 d	187 ± 31 d	2466 ± 353 d	48.38 ± 5.27 c	36.42 ± 6.93 c	6.12 ± 1.01 d	5.84 ± 0.87 c
	179.49	3539 ± 483 a	49 ± 8 b	226 ± 35 b	3264 ± 450 a	46.08 ± 4.59 d	32.07 ± 6.41 de	6.90 ± 1.09 c	7.11 ± 0.95 a
	211.45	2871 ± 445 c	39 ± 8 d	200 ± 38 c	2633 ± 407 c	45.48 ± 5.20 de	33.01 ± 6.99 d	6.71 ± 1.13 c	5.75 ± 0.95 c
	229.68	3293 ± 355 b	43 ± 7 c	223 ± 27 b	3028 ± 331 b	44.57 ± 3.40 e	30.85 ± 4.74 e	7.29 ± 0.96 b	6.43 ± 0.73 b
	274.58	2219 ± 270 e	54 ± 9 a	237 ± 41 a	1929 ± 228 e	42.42 ± 3.75 f	27.70 ± 5.82 f	9.10 ± 1.52 a	5.62 ± 0.76 c
Silty clay	50.41	1657 ± 107 g	12 ± 4 g	85 ± 11 g	1560 ± 102 e	50.23 ± 3.14 a	43.33 ± 3.18 a	3.09 ± 0.44 f	3.82 ± 0.37 f
	59.47	4600 ± 610 a	30 ± 6 d	177 ± 25 d	4393 ± 587 a	47.12 ± 5.46 b	36.12 ± 6.73 b	4.77 ± 0.66 d	6.22 ± 0.87 b
	65.98	2287 ± 444 f	21 ± 9 f	120 ± 36 f	2147 ± 412 d	45.57 ± 5.02 c	36.45 ± 6.80 b	4.42 ± 1.39 e	4.71 ± 0.94 e
	88.12	3053 ± 354 d	27 ± 7 e	130 ± 24 e	2896 ± 344 c	46.24 ± 7.28 bc	36.53 ± 8.12 b	4.58 ± 0.85 de	5.13 ± 0.54 d
	93.69	3798 ± 229 b	40 ± 6 b	226 ± 21 b	3533 ± 222 b	44.67 ± 2.74 cd	30.60 ± 3.36 c	6.84 ± 0.71 b	7.24 ± 0.42 a
	119.17	3228 ± 380 c	38 ± 7 c	189 ± 29 c	3000 ± 362 c	43.41 ± 4.27 d	30.91 ± 5.62 c	6.36 ± 1.04 c	6.13 ± 0.69 b
	141.02	2404 ± 518 e	50 ± 10 a	245 ± 62 a	2109 ± 455 d	40.90 ± 7.73 e	26.18 ± 10.96 d	9.01 ± 2.16 a	5.71 ± 1.26 c
	269.72	3788 ± 387 b	36 ± 5 c	230 ± 26 b	3521 ± 369 b	38.19 ± 2.89 f	23.67 ± 4.03 e	7.12 ± 0.80 b	7.40 ± 0.80 a

Results are given as mean ± standard deviation. Within columns, values followed by the same letter for soil type or depth are not significantly different at the 0.05 level (LSD)

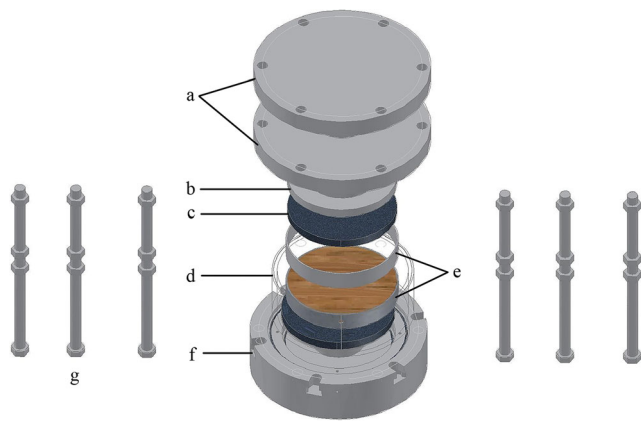


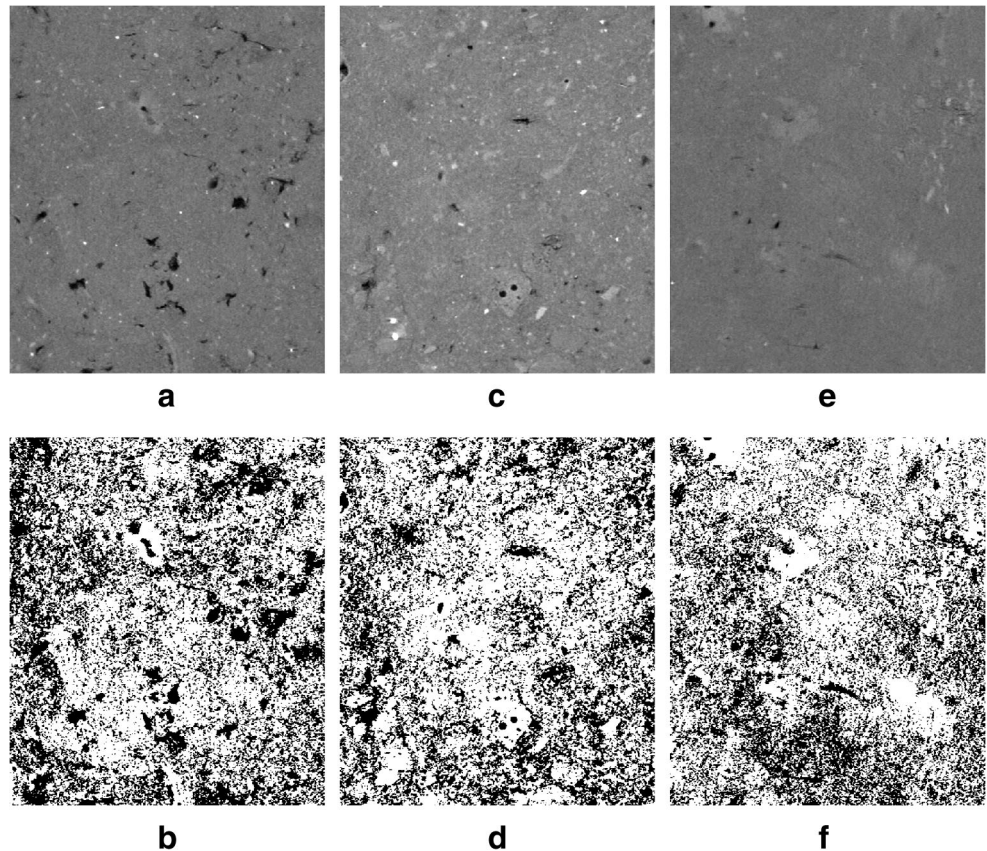
**Fig. 2** Compression device allowing for sample compression and X-ray micro-CT scanning at a strain-locked state. The design included a pressure cap, **b** top plate, **c** porous stone, **d** transparent outer cylinder, **e** Plexiglas ring and guard ring containing the sample, **f** bottom plate, and **g** pressure bar

### 2.3 Analysis of pore morphology

Circularity is commonly used to represent pore morphology. Pore circularity was obtained by the following equation (Tuller et al. 1999):

$$C = \frac{4\pi(A_p)}{(P_p)^2} \tag{2}$$

**Fig. 3** Rectangular 72.71 mm<sup>2</sup> (7.88 mm × 9.23 mm) area 8-bit grayscale images and binary images of **a, b** clay, **c, d** silt, and **e, f** silty clay



where  $A_p$  and  $P_p$  are the pore area and perimeter, respectively. A circularity of 1 indicates that the pore is perfectly circular, whereas a smaller value suggests that the pore is elongated and non-circular (Udawatta et al. 2006). According to Pagliai et al. (2004), soil pores were divided into three classes defined by the shape factor  $F$  (corresponding to the reciprocal of circularity): regular pores ( $1 < F < 2$ ), irregular pores ( $2 < F < 5$ ), and elongated pores ( $F > 5$ ). The regular pore area, irregular pore area, and elongated pore area of an image was divided by the 72.71 mm<sup>2</sup> total area to calculate regular porosity, irregular porosity, and elongated porosity, respectively.

To better characterize the shape of the pore's space, the structure model index (SMI) was introduced according to Hildebrand and R uegsegger (1997):

$$SMI = 6 \times \frac{V \times \left(\frac{dS}{dr}\right)}{S^2} \tag{3}$$

where  $V$  and  $S$  are the (triangulated) pore volume and surface, respectively, and  $dS/dr$  is the surface area derivative. The SMI acquires values of 0 (ideal plates), 3 (cylinders), and 4 (spheres), and intermediate values for objects composed of intermediate or irregular shapes.

The degree of anisotropy (DA) is a measure of orientation of a structure within a volume. It is a calculated geometric characteristic and usually defined as the ratio of the maximum

and minimum radius of the mean intercept length tensor (Harrigan and Mann 1984). The DA ranges from 0 (perfectly isotropic) to 1 (anisotropic).

The connectivity of the pore system was quantified with the Euler number (the volumetric Euler-Poincaré characteristic, hereafter  $E_v$ ) according to Dal Ferro et al. (2013). The smaller the  $E_v$ , the better the connectivity of the pore system. Pore connectivity affects water flow and solute transport in the soil.

SMI, DA, and  $E_v$  were calculated using the ImageJ BoneJ plug-in. The theoretical background and methodological details of the image analysis required for their calculation are described elsewhere (Doube et al. 2010; Dal Ferro et al. 2013; Zhao et al. 2017b).

## 2.4 Statistical analysis

The results are expressed as means  $\pm$  standard deviations. Significant differences in pore characteristics and pore morphological parameters among soil types and soil depths were analyzed with one-way ANOVA and Fisher's test, calculated at  $P=0.05$ . Pearson correlation analysis was used to determine the relationships among various parameters. All statistical analyses used SPSS version 19.0 at  $P=0.05$ .

## 3 Results

### 3.1 Visualization of pore networks

Three-dimensional visualizations of pores in clay, silt, and silty clay soils at a depth of about 165 m are shown in Fig. 4. Spatial pore characteristics differed clearly between different soil types. In particular, the number of micropores was much lower in silt (Fig. 4b) and silty clay (Fig. 4c) soils than in clay soil (Fig. 4a), whereas the proportion of macropores was higher in silt soil than in the other two soil

types. The pores of clay soil were also less tortuous and smoother.

### 3.2 CT-measured porosity, macroporosity, coarse mesoporosity, and microporosity

CT-measured porosity and macroporosity were significantly higher in silt (116.03%, 138.99%) and silty clay (106.46%, 123.13%) soils than in clay soil, while CT-measured coarse mesoporosity was significantly lower in silt (76.63%) and silty clay (71.86%) soils than in clay soil ( $P<0.05$ ; Fig. 5a–c, Table 1). The difference in microporosity was not obvious.

CT-measured porosity and macroporosity were significantly affected by soil depth ( $P<0.05$ ; Fig. 5a, b, Table 1). Within the soil depth, silt soil exhibited the greatest porosity followed by silty clay and clay soils; moreover, the same trend was observed for macroporosity, except for the last depth of clay soil. This finding indicated a strong correlation between porosity and macroporosity (Table S2 - ESM). For silt soil, porosity was higher at the top depth of 37.45 m ( $53.48 \pm 4.98\%$ ) and decreased to  $42.42 \pm 3.75\%$  at the deepest depth of 274.58 m, corresponding to a total decline of 20.68%, whereas macroporosity decreased from  $44.97 \pm 6.24\%$  to  $27.70 \pm 5.82\%$ , resulting in a 38.40% drop. For silty clay soil, porosity dropped by 23.97% and macroporosity by 45.37%, respectively. Finally, for clay soil, porosity decreased by 8.12%, whereas macroporosity showed a slight increase (Fig. 5a, b, Table 1).

CT scans revealed that coarse mesoporosity and microporosity were also significantly affected by soil depth ( $P<0.05$ ; Fig. 5c, d, Table 1). Coarse mesoporosity (and microporosity) of silt and silty clay soils showed a tendency to increase with increasing depth, reaching 1.36 (0.21) and 1.30 (0.94) times greater values, respectively, at the deepest point compared to the top. In contrast, clay soil displayed no obvious trend.

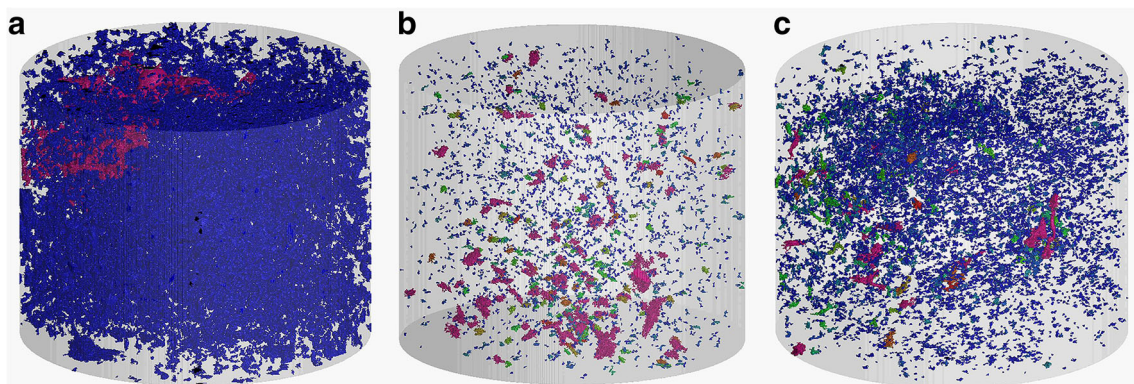
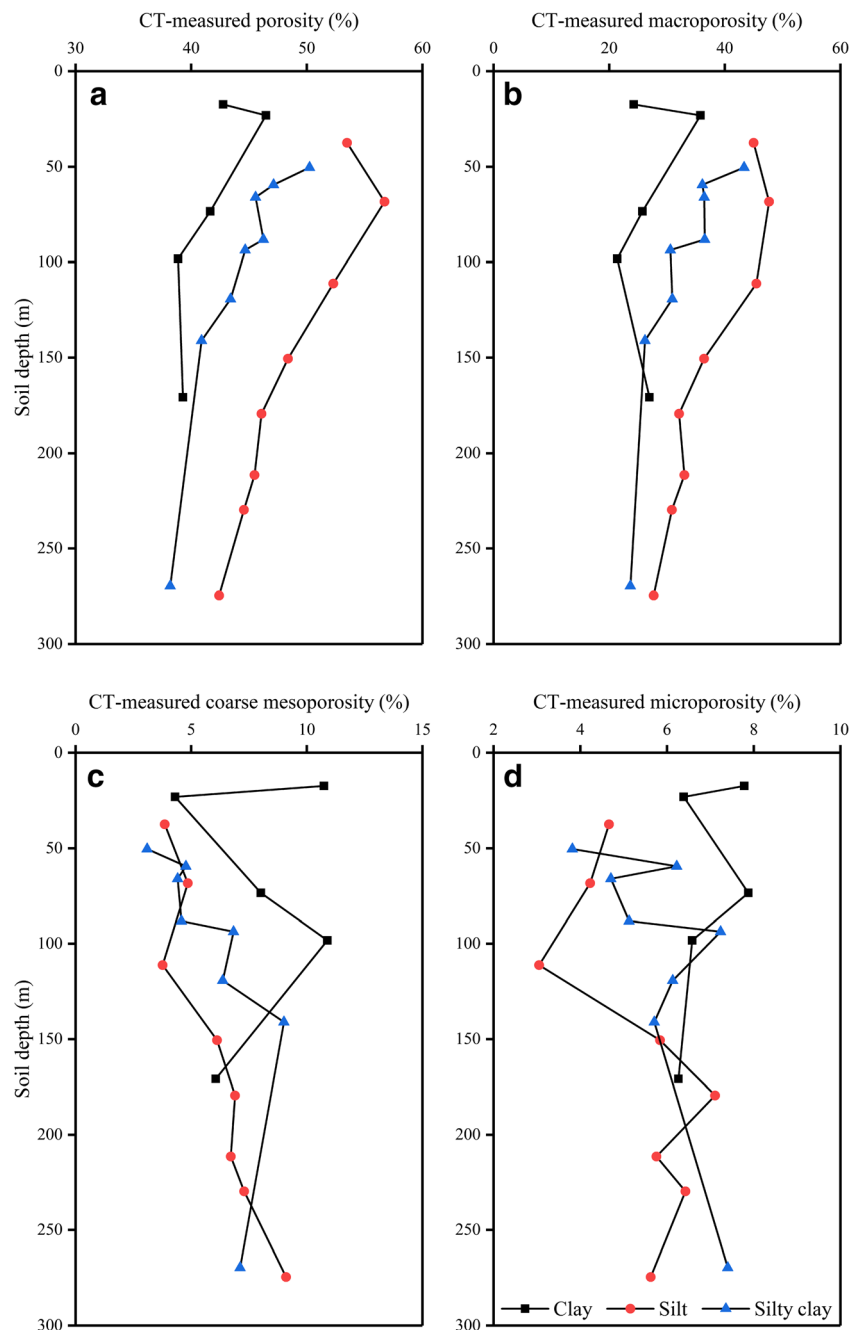


**Fig. 4** Three-dimensional visualization of soil pore networks in the soil columns under **a** clay, **b** silt, and **c** silty clay. The blue is micropore and the red is macropore

**Fig. 5** CT-measured **a** porosity, **b** macroporosity, **c** coarse mesoporosity, and **d** microporosity for clay, silt, and silty clay soils by depth

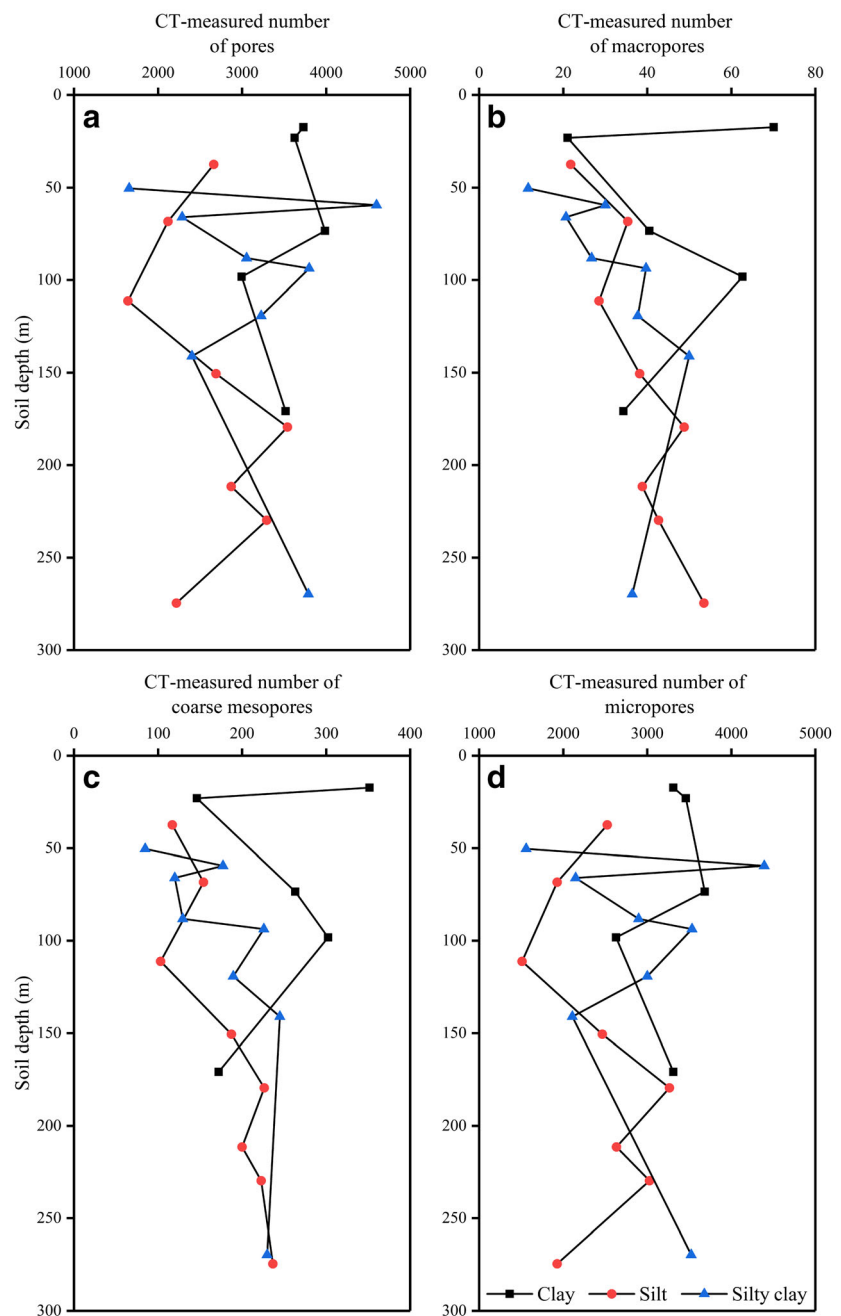


### 3.3 CT-measured number of pores

The distribution of the number of CT-measured pores were significantly different between soil types and depths ( $P < 0.05$ ; Fig. 6a, Table 1). The average for clay, silt, and silty clay soils across all depths was  $3571 \pm 367$ ,  $2630 \pm 625$ , and  $3102 \pm 960$  pores on a  $72.71 \text{ mm}^2$  scan area, respectively (Table 1). Compared with clay soil, the number of pores for silt and silty clay soils were respectively 0.74 and 0.87 times. The maximum number of pores in clay soil was  $3988 \pm 464$  at a depth of 73.42 m; whereas for silt and silty clay soils, the

maximum numbers were  $3539 \pm 483$  (197.49 m) and  $4600 \pm 610$  (59.47 m), respectively (Table 1). The number of CT-measured pores (macropores, coarse mesopores, and micropores) in clay soil decreased from  $3731 \pm 283$  at 17.32 m to  $3517 \pm 453$  at 170.78 m, corresponding to a decline of 5.74%. The drop was larger for silt soil, with the number decreasing from  $2663 \pm 299$  at 37.45 m to  $2219 \pm 270$  at 274.58 m, which corresponded to a decline of 16.67%. In contrast, for silty clay soil, pore numbers increased by 128.61%, from  $1657 \pm 107$  at 50.41 m to  $3788 \pm 387$  at 269.72 m (Table 1). The rate at which the number of pores changed with increasing soil depth

**Fig. 6** Number of CT-measured (a) pores, (b) macropores, (c) coarse mesopores, and (d) micropores for clay, silt, and silty clay soils by depth



was basically the same for clay and silt soils and gradually decreased for silty clay soil (Fig. 6a). Generally, silt soil had fewer pores than clay soil within the studied depth, while for silty clay soil the pore numbers varied greatly.

The number of CT-measured macropores was also significantly influenced by soil type and soil depth ( $P < 0.05$ ; Fig. 6b, Table 1). On average, clay, silt, and silty clay soils had  $46 \pm 20$ ,  $38 \pm 10$ , and  $32 \pm 12$  macropores across all study depths (Table 1). The number of macropores in clay soil decreased with soil depth by nearly half from the top to the lowest depth; conversely, the corresponding value of silt and

silty clay soils increased by 1.45 and 2.00 times (Table 1). The number of macropores in the three soil types was relatively close between 23 and 59 m, it then increased most for clay soil, followed by silty clay and silt soils, between 59 and 141 m, and was finally similar for silt and silty clay soils below 141 m (Fig. 6b).

The number of CT-measured coarse mesopores varied similarly to that of macropores, and was also significantly affected by soil type and soil depth ( $P < 0.05$ ; Fig. 6c, Table 1). Clay soil had  $247 \pm 87$  coarse mesopores across all study depths on a  $72.71 \text{ mm}^2$  scan area as compared to  $181 \pm 51$  and  $175 \pm 58$



in silt and silty clay soils, respectively (Table 1). The number of coarse mesopores in silt and silty clay soils were 0.73 and 0.71 times than that in clay soil. As with macropores, coarse mesopore numbers in clay soil decreased by almost half from the top depth to the deepest point. Instead, in silt and silty clay soils, the number of coarse mesopores increased 1.03 and 1.71 times within the studied depths (Table 1). Between 37 and 88 m, coarse mesopore numbers in silt and silty clay soils were close to each other; between 88 and 141 m, the order of coarse mesopore numbers was clay>silty clay>silt; after that, values were similar for silt and silty clay soils (Fig. 6c).

Soil type and soil depth had a significant effect on the number of CT-measured micropores ( $P < 0.05$ ; Fig. 6d, Table 1), and the trend reflected that observed for CT-measured pores. On average across all depths, clay, silt, and silty clay soils had  $3278 \pm 394$ ,  $2410 \pm 591$ , and  $2895 \pm 927$  pores on a  $72.71 \text{ mm}^2$  scan area, respectively (Table 1). Thus, the number of micropores in silt and silty clay soils was 0.74 and 0.88 times than that of clay soil,

respectively. The number of micropores in clay soil was basically the same at the top and the lowest depth, but the value first increased, then decreased, and then increased again. In silt soil, micropore numbers decreased from  $2525 \pm 276$  (37.45 m) to  $1929 \pm 228$  (274.58 m), corresponding to a drop of 23.6%. As with pores, in silty clay soil, micropore numbers increased by 1.26 times. Generally, silt soil had fewer micropores than clay soil within the studied depth; however, micropore numbers varied greatly for silty clay soil.

### 3.4 Pore morphology of soil

The morphological parameters examined in this study were circularity, shape factor, SMI, DA, and Ev. The soil type had no significant effect on circularity ( $P > 0.05$ ; Table 2), as the average values of clay ( $0.804 \pm 0.035$ ) and silt ( $0.806 \pm 0.021$ ) soils were similar and only slightly lower than that of silty clay ( $0.824 \pm 0.027$ ) soil. Pore circularity, however, was

**Table 2** CT-measured pore circularity, structure model index (SMI), degree of anisotropy (DA), and the Euler number (Ev) as influenced by clay, silt, and silty clay soil types and depth ( $n = 21$ )

	Depth (m)	Circularity	Structure model index (SMI)	Degree of anisotropy	Euler number ( $10^{-5} \text{ pixel}^{-3}$ )
<b>Soil type means</b>					
Clay		$0.804 \pm 0.035$ a	$2.274 \pm 1.174$ a	$0.344 \pm 0.093$ a	$8.702 \pm 6.239$ b
Silt		$0.806 \pm 0.021$ a	$1.409 \pm 1.424$ b	$0.360 \pm 0.078$ a	$13.011 \pm 4.394$ a
Silty clay		$0.824 \pm 0.027$ a	$2.008 \pm 1.366$ ab	$0.395 \pm 0.092$ a	$7.090 \pm 2.680$ b
<b>Depth means</b>					
Clay	17.32	$0.767 \pm 0.005$ e	3.357	0.201	17.53
	23.05	$0.839 \pm 0.008$ a	0.370	0.396	1.68
	73.42	$0.804 \pm 0.005$ c	2.069	0.296	9.53
	98.20	$0.772 \pm 0.009$ d	3.049	0.407	10.87
	170.78	$0.836 \pm 0.010$ b	2.516	0.412	3.9
Silt	37.45	$0.843 \pm 0.006$ a	0.076	0.376	9.35
	68.25	$0.799 \pm 0.009$ d	0.094	0.241	23.22
	111.12	$0.828 \pm 0.019$ b	0.267	0.492	13.21
	150.50	$0.796 \pm 0.007$ e	0.619	0.383	11.85
	179.49	$0.801 \pm 0.006$ d	2.538	0.265	13.62
	211.45	$0.806 \pm 0.008$ c	1.250	0.403	9.54
	229.68	$0.805 \pm 0.006$ c	2.511	0.345	11.77
	274.58	$0.772 \pm 0.009$ f	3.915	0.380	11.53
	Silty clay	50.41	$0.847 \pm 0.008$ a	3.827	0.516
59.47		$0.837 \pm 0.005$ c	0.587	0.269	5.52
65.98		$0.842 \pm 0.014$ b	0.327	0.442	4.74
88.12		$0.849 \pm 0.014$ a	0.632	0.444	7.19
93.69		$0.811 \pm 0.007$ e	1.404	0.301	10.28
119.17		$0.820 \pm 0.010$ d	2.437	0.398	9.52
141.02		$0.767 \pm 0.011$ f	3.857	0.481	9.44
269.72		$0.811 \pm 0.006$ e	2.983	0.308	7.47

Results are given as mean  $\pm$  standard deviation. Within columns, values followed by the same letter for soil type or depth are not significantly different at the 0.05 level (LSD)

significantly different at the various depths examined ( $P < 0.05$ ; Fig. 7a, Table 2). In clay soil, circularity varied from  $0.767 \pm 0.005$  to  $0.836 \pm 0.010$  at the top (17.32 m) to the last (170.78 m) sampled depth. In silt (and silty clay) soil, it varied from  $0.843 \pm 0.006$  ( $0.847 \pm 0.008$ ) at 37.45 m (50.41 m) to  $0.772 \pm 0.009$  ( $0.811 \pm 0.006$ ) at 274.58 m (269.72 m). In all three soil types, circularity showed repeated increase and decrease, but the overall tendency was for clay soil to increase, and for silt and silty clay soils to decrease.

The proportions of regular, irregular, and elongated pores within each soil type are shown in Fig. 7b–d. Soil type had a significant effect on the proportion of various pore shapes ( $P < 0.05$ ; Table 3). The fraction of elongated pores was highest in silt soil (84.22%), followed by silty clay soil (81.95%), and the lowest in clay soil (76.06%). Stress (increasing soil depth) exerted also a significant influence on proportions of pore shape ( $P < 0.05$ ; Fig. 7b–d, Table 3). Elongated pores in silt and silty clay soils decreased with increasing depth, whereas regular and irregular porosity increased. For clay soil, the proportions of regular, irregular, and elongated pores fluctuated greatly with depth.

SMI was highest in clay soil (on average 2.274), followed by silty clay soil (on average 2.008), and the lowest in silt soil (on average 1.409). SMI increased with increasing depth for silt and silty clay soils, but it fluctuated with depth in clay soil (Fig. 8a).

DA was greatest in silty clay soil (on average 0.395), followed by silt soil (on average 0.360), and the lowest in clay soil (on average 0.344). DA of the pore network revealed a slight orientation of the pores; however, DA did not differ significantly among soil types ( $P > 0.05$ ; Table 2). With the increase in depth, DA doubled in clay soil (from 0.201 to 0.412), whereas the other two soil types showed a tendency to fluctuate or even decrease (Fig. 8b, Table 2).

Ev was significantly lower in clay (66.88%) and silty clay (54.49%) soils than in silt soil ( $P < 0.05$ ; Table 2). The value in silt and silty clay soils generally increased with increasing depth, especially in silty clay soil, which is nearly four times than its initial value, while in the clay soil, it appeared to fluctuate back and forth (Fig. 8c, Table 2).

### 3.5 Correlation analysis of parameters

Correlation analysis of soil pore characteristics and morphological parameters using data from all soil samples and three different soil types is shown in Table S2 (ESM). Significant positive correlations were found for number of pores, number of micropores, and number of regular pores ( $P < 0.01$ ) as well as for number of macropores, number of coarse mesopores, and number of elongated pores ( $P < 0.01$ ). In addition, macroporosity exhibited a significant positive correlation with porosity and elongated porosity ( $P < 0.01$ ), whereas there was a significant negative correlation with regular porosity and

**Fig. 7** a Pore circularity values at the study depths for clay, silt, and silty clay soils; and pore shape porosity at the study depths for b clay, c silt, and d silty clay soils. Different letters following values between the same shape type indicate significant difference at the 0.05 level (LSD). Error bars indicate the standard error

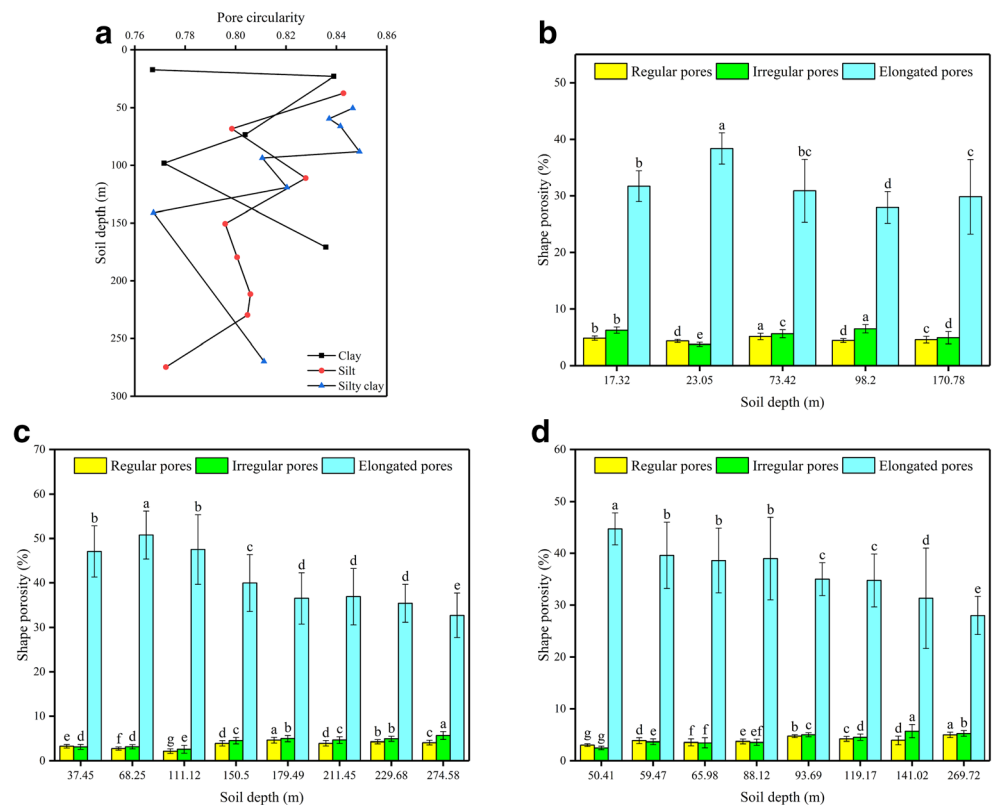


**Table 3** CT-measured number of pores and porosity for different pore shapes (regular, irregular, and elongated) as influenced by clay, silt, and silty clay soil types and depth ( $n = 21$ )

	Depth (m)	Number			Porosity (%)		
		Regular pores	Irregular pores	Elongated pores	Regular porosity	Irregular porosity	Elongated porosity
Soil type means							
Clay		2936 ± 360 a	470 ± 83 a	165 ± 70 a	4.60 ± 0.55 a	5.40 ± 0.89 a	31.80 ± 3.77 b
Silt		2167 ± 517 b	343 ± 94 c	119 ± 34 b	3.63 ± 0.92 b	4.25 ± 1.17 b	41.00 ± 6.74 a
Silty clay		2619 ± 811 ab	371 ± 131 b	112 ± 46 b	4.13 ± 0.64 ab	4.13 ± 1.25 b	36.50 ± 5.40 ab
Depth means							
Clay	17.32	2896 ± 217 d	572 ± 56 a	263 ± 22 a	4.83 ± 0.39 b	6.24 ± 0.56 b	31.69 ± 2.74 b
	23.05	3134 ± 205 b	400 ± 43 d	91 ± 11 e	4.34 ± 0.27 d	3.75 ± 0.35 e	38.38 ± 2.77 a
	73.42	3280 ± 385 a	538 ± 68 b	170 ± 23 c	5.14 ± 0.56 a	5.62 ± 0.71 c	30.90 ± 5.58 bc
	98.20	2344 ± 175 e	454 ± 50 c	196 ± 16 b	4.41 ± 0.33 d	5.49 ± 0.75 a	27.96 ± 2.81 d
Silt	170.78	3027 ± 412 c	385 ± 46 e	105 ± 14 d	4.56 ± 0.59 c	4.91 ± 1.09 d	29.83 ± 6.62 c
	37.45	2311 ± 249 c	281 ± 42 e	71 ± 17 f	3.29 ± 0.40 e	3.12 ± 0.55 d	47.07 ± 5.79 b
	68.25	1723 ± 217 e	283 ± 41 e	112 ± 22 e	2.76 ± 0.36 f	3.18 ± 0.48 d	50.78 ± 5.44 a
	111.12	1389 ± 282 f	185 ± 63 f	69 ± 30 f	2.17 ± 0.53 g	2.60 ± 0.89 e	47.52 ± 7.89 b
Silty clay	150.50	2196 ± 311 d	376 ± 60 c	119 ± 22 d	3.91 ± 0.56 d	4.49 ± 0.69 c	39.98 ± 6.39 c
	179.49	2899 ± 397 a	479 ± 70 a	162 ± 25 a	4.61 ± 0.61 a	4.95 ± 0.69 b	36.52 ± 5.80 d
	211.45	2365 ± 356 c	379 ± 70 c	128 ± 25 c	3.93 ± 0.59 d	4.65 ± 0.73 c	36.90 ± 6.36 d
	229.68	2710 ± 293 b	434 ± 52 b	149 ± 20 b	4.26 ± 0.46 b	4.90 ± 0.56 b	35.41 ± 4.26 d
	274.58	1748 ± 200 e	328 ± 53 d	143 ± 24 b	4.07 ± 0.50 c	5.64 ± 0.91 a	32.71 ± 5.02 e
	50.41	1459 ± 91 f	161 ± 21 f	36 ± 7 f	3.03 ± 0.27 g	2.49 ± 0.33 g	44.72 ± 3.10 a
	59.47	3936 ± 520 a	519 ± 78 a	145 ± 22 b	3.86 ± 0.53 d	3.65 ± 0.53 e	39.60 ± 6.44 b
	65.98	1989 ± 375 d	237 ± 59 e	61 ± 23 e	3.53 ± 0.65 f	3.45 ± 0.95 f	38.59 ± 6.30 b
	88.12	2674 ± 334 c	298 ± 39 d	80 ± 16 d	3.71 ± 0.43 e	3.55 ± 0.58 ef	38.98 ± 8.02 b
	93.69	3152 ± 204 b	494 ± 33 b	152 ± 14 ab	4.71 ± 0.29 b	4.97 ± 0.39 c	34.99 ± 3.19 c
	119.17	2716 ± 331 c	388 ± 50 c	124 ± 20 c	4.18 ± 0.47 c	4.48 ± 0.60 d	34.75 ± 5.14 c
	141.02	1877 ± 396 e	376 ± 93 c	152 ± 37 ab	3.91 ± 0.81 d	5.67 ± 1.30 a	31.32 ± 9.72 d
269.72	3146 ± 325 b	495 ± 58 b	147 ± 17 b	4.96 ± 0.53 a	5.23 ± 0.55 b	28.00 ± 3.67 e	

Results are given as mean ± standard deviation. Within columns, values followed by the same letter for soil type or depth are not significantly different at the 0.05 level (LSD)

irregular porosity. There was a highly significant correlation between coarse mesoporosity and irregular porosity ( $P < 0.01$ ), and a significant correlation between microporosity and regular porosity ( $P < 0.05$ ). SMI (and thereby the fraction of spherical pores) increased with decreasing macroporosity ( $r = -0.72$ ; Table S2 - ESM). Instead, the relationships between DA and porosity and between DA and macroporosity were less clear. These findings are consistent with those of Schäffer et al. (2007).

## 4 Discussion

### 4.1 Soil pore characteristics

Porosity is a key property of soil structure, which affects water transport capacity and thereby the loss of nutrients

during runoff. As a result, it has been used widely as a measure of the soil’s aeration and infiltration capacity (Udawatta et al. 2008). According to Terzaghi (1943), a direct correlation between coefficient of consolidation and porosity indicates that porosity is closely related to soil compaction. In all soil samples examined in this study, porosity correlated highly with macroporosity, suggesting that porosity is dominated by macropores (Table S2 - ESM). Macropores accounted for 55% to 77% of total porosity in clay soil, 65% to 87% in silt soil, and 62% to 86% in silty clay soil. Visualization of pore networks confirmed the higher proportion of macropores in silt and silty clay soils than in clay soil (Fig. 4). Analyzing the change in porosity and macroporosity with depth, both decreased in silt and silty clay soils, whereas coarse mesoporosity and microporosity increased with increasing depth, and no obvious trend was observed for clay soil.

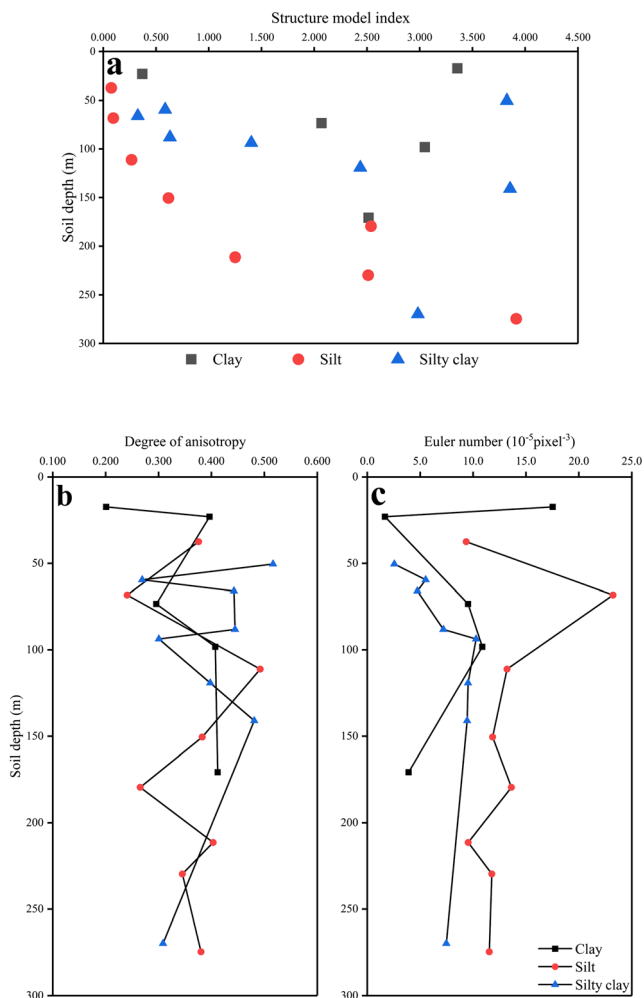


**Fig. 8** a Structure model index (SMI), b degree of anisotropy, and c the Euler number for clay, silt, and silty clay soils by depth

These findings suggest that the ability of compression is greater in silt and silty clay soils than that in clay soil.

Soil tillage and compaction normally decrease soil macroporosity and alter PSD (Cássaro et al. 2011; Lipiec et al. 2012; da Costa et al. 2014). Kim et al. (2010) reported that porosity and macroporosity of Mexico's silt loam decreased by 65% and 64%, respectively, due to soil compression. This value is larger than that calculated in this paper, which may be partly explained by the study's deeper sampling depth and thus lower compressibility. Gu et al. (2018) found that mechanical compression affected only macropores. Here, the reason for the increment in microporosity and coarse mesoporosity at a relatively greater depth may be linked to some macropores being transformed into micropores or coarse mesopores. This might have occurred because of fractures or area reduction, hence augmenting the volume of micropores and coarse mesopores. A higher proportion of macropores in soil microstructures favors land subsidence; therefore, determination of the proportions of macropores in deformable strata allows the estimation of land subsidence potential (Gu et al.

2018). Wu et al. (2008) reported that the deformation of each soil layer was due not only to its compressibility but also to its thickness. In this study, porosity of silt soil ( $R^2 = 0.9068$ ) and silty clay soil ( $R^2 = 0.8275$ ) decreased linearly with depth; whereas in clay soil ( $R^2 = 0.6659$ ), it showed a logarithmic decrease with depth (Fig. S2 - ESM). These findings indicate that the pores become greatly reduced, particularly in silt and silty clay soils. Combined with borehole data, silt and silty clay soils accounted for 20.11% (23.00%) and 30.76% (28.86%) of overall soil in YHG-1 (YHG-2), and had relatively large thickness. Therefore, the main contributors to land subsidence in this region are silt and silty clay soils. This was expected, as larger pores are generally more easily compacted than smaller ones (Gupta et al. 1989), and the proportion of macropores is high in these soil types. The porosity of clay soil did not change much when it reaches a certain depth, which could be partly attributed to the large portion of micropores that are not easily compressed.

The variation in the number of CT-measured pores and micropores was similar in all soil types, and the strong correlation between these values indicates that pore numbers were determined mainly by micropore numbers. In addition, there was a good correlation between the number of CT-measured macropores and coarse mesopores (Table S2 - ESM). Micropores accounted for 87% to 95% of total pores. In the study by Kim et al. (2010), the number of macropores and coarse mesopores in Mexico's silt loam was reduced by 69% and 75% under compression, respectively. This is similar to the effect of compaction caused by the increase in depth for clay soil observed in this study. Here, clay soil displayed the largest number of CT-measured pores among three soil types analyzed; presumably, this was due to its high number of micropores, which are not easy to compact (Gupta et al. 1989). The number of CT-measured macropores and coarse mesopores in silt and silty clay soils showed a tendency to increase with depth, whereas total porosity and macroporosity decreased. This suggests that some of the large macropores in these two soil types fractured into relatively small macropores and coarse mesopores, accompany with the macropores altered from long to short (Wang et al. 2019). This further indicates that land subsidence caused by silt and silty clay soils is due to the compression or even destruction of macropores.

#### 4.2 Pore morphology of soil

The closer circularity is to 1.0, the closer the pore is to a circular shape. If two areas are similar, then the pore with a more irregular surface will have a higher measured perimeter and a lower circularity value (Rachman et al. 2005). The circularity of clay soil increased with depth, while it decreased in silt and silty clay soils. This suggests that the pores in clay soil tended to be more circular with increasing depth (Li et al. 2016; Rachman et al. 2005), which could be partly attributed

to the large number of micropores, as smaller pores have a larger probability of being round (Lebron et al. 2002). The decrement in circularity in silt and silty clay soils further confirms that the large macropores in these two soil types transformed into relatively small macropores and coarse mesopores with increasing depth. The randomness of the conversion made the pores slightly irregular; however, the overall difference remained small.

As shown in Table S2 (ESM), there was a significant positive correlation between macroporosity and elongated porosity ( $P < 0.01$ ), and a negative correlation with regular and irregular porosity. The correlation coefficients between coarse mesoporosity and irregular porosity, microporosity and regular porosity, and micropore numbers and regular pore numbers were 0.91 ( $P < 0.01$ ), 0.89 ( $P < 0.05$ ), and 0.99 ( $P < 0.01$ ), respectively. This indicates that macropores were mostly elongated, coarse mesopores were mostly irregular, and micropores were generally more regular (Zhao et al. 2017a). Our study also supports the conclusion that macroporosity is more sensitive to the fraction of elongated pores which have been reported by Ma et al. (2015) and Zhao et al. (2017a).

Here, elongated pores dominated total porosity (on average 80.81%) in all soil samples, which is similar to the result (80%) obtained by Zhao et al. (2017b). The fractions of elongated pores were significantly higher in silt and silty clay soils than in clay soil (Table 3), as confirmed also by visualization of pore networks (Fig. 4). As depth increases, the fractions of elongated pores in silt and silty clay soils decrease, while the fractions of regular and irregular pores increase, and the correlation coefficient between total porosity and elongated porosity is 0.92 ( $P < 0.01$ ; Table S2 - ESM). Accordingly, the observed significant reduction in porosity with increasing depth can be attributed to a reduction in the volume of elongated macropores (Pagliai et al. 2003; Pagliai et al. 2004; Zhao et al. 2017a). In addition, elongated pores, which have high transport capacity for water and gases, are defined as transmission pores (Zhao et al. 2017a). As drainage progresses, water pressure in elongated pores dissipates and the pores are compressed, augmenting the chance of fracture. Pachepsky et al. (1996) proposed that a decrease in elongated porosity inhibited water transport, causing the friction between soil particles to give in to compaction, and the soil to be pressed with a negative vertical displacement. Gu et al. (2018) suggested that strata, which contributed to larger deformations during land subsidence, tended to exhibit larger shape factors due to the presence of elongated macropores. Therefore, we conclude that the reduction in elongated macropores in silt and silty clay soils is likely the main cause of soil compaction and even land subsidence.

SMI was small in silt soil above 150 m and silty clay soil above 90 m, indicating that the pores in these two soil types were mostly plate-shaped when the stress was small, and then changed gradually to cylindrical and spherical with increasing

soil depth. The increase in SMI with growing depth for silt and silty clay soils indicates that the number of spherical pores increased compared to the number of cylindrical pores due to elongated macropores' collapse (Naveed et al. 2016). Schäffer et al. (2007) also reported an increase in the fraction of spherical pores under increasing compaction. The DA exhibited no obvious change in silt and silty clay soils with increasing depth, indicating that compaction had only a minor effect in inducing preferential orientation of the pores (Schäffer et al. 2008). The Ev further indicates that pore connectivity in silt and silty clay soils decreased with increasing depth, which was due to the loss of elongated macropores (Naveed et al. 2016).

### 4.3 Pore size distribution and pore deformation pattern

Critical analyses of PSD allows for a more detailed understanding of the changes on soil structure in the region of macro, meso, and micropores (Kutlílek 2004). Therefore, in principle, a more representative analysis of soil structure complexity and modifications can be made using this approach. In our study, PSD varied not only in the type of soils but also at the various depth (Fig. 9). PSD of pores with diameter  $< 1$  mm shows that most pores in this range had a diameter  $< 0.2$  mm (micropores). In addition, Fig. 9 shows cumulative PSD sorted by porosity in each soil sample. Within the same soil type, cumulative PSD was about the same for pores with diameter  $< 0.02$  mm, but the difference increased with pore diameter (Fig. 9b, d, f), indicating that depth (increasing stress) significantly altered PSD of soil. The variation in pore deformation patterns with depth of different soil types is shown in Fig. 10. We suggest two categories of pore deformation patterns: (1) elongated or irregular macropores or coarse mesopores fracture and transform into macropores, coarse mesopores, and micropores with relatively small diameters; (2) the whole compression process causes macropores to become coarse mesopores, coarse mesopores become micropores, and micropores tend to close. It is worth noting that the variation of coarse mesopores and micropores depends on the difference between the self-compression value and the value obtained by macropore collapse in any deformation pattern; moreover, the closure of micropores is always present. According to Xie et al. (2018) and Wang et al. (2019), some soil particles may be crushed under a high stress level, changing the position of other soil particles and deforming the pore space. However, how this occurs exactly remains unclear.

More than 60% of the pore volume consisted of macropores with diameter  $> 1000$   $\mu\text{m}$  for all soil samples (64.11% for clay soil, 76.80% for silt soil, and 74.16% for silty clay soil). At increasing depths, such as 98.20 to 170.78 m (clay soil), 111.12 to 150.50 m (silt soil), and 141.02 to 269.72 m (silty clay soil), the peak of PSD of coarse

**Fig. 9** Changes in pore size distribution of coarse mesopores and micropores, and changes in cumulative pore size distribution for **a, b** clay, **c, d** silt, and **e, f** silty clay soils with increasing depth

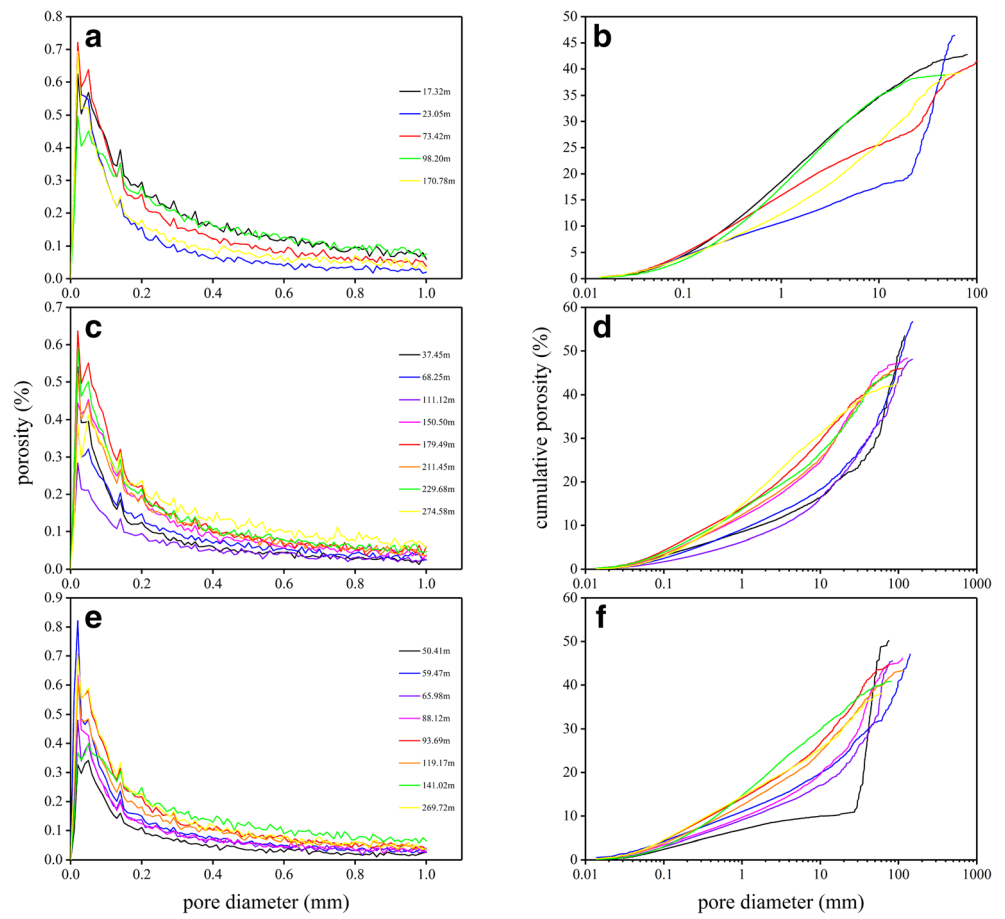
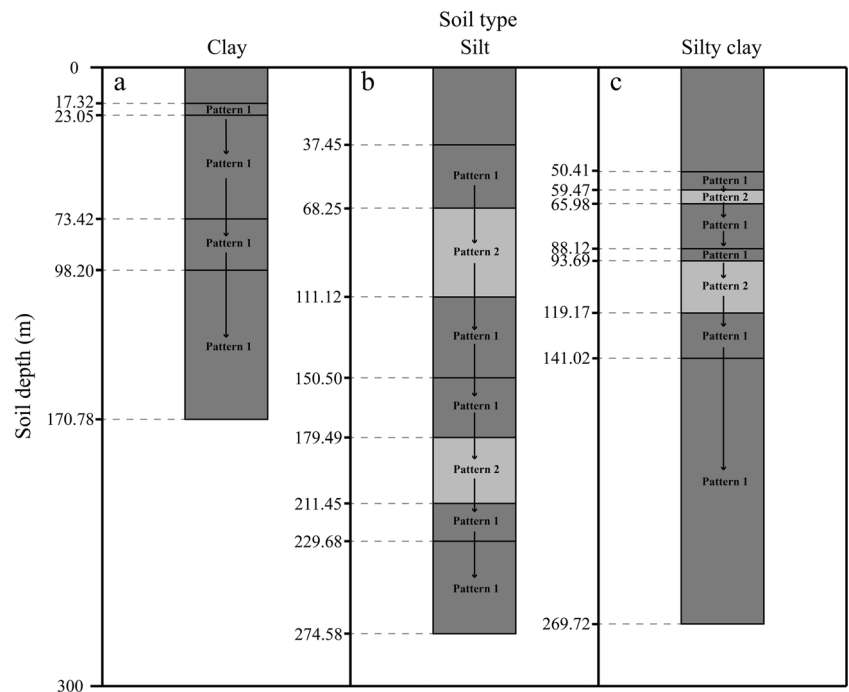


**Fig. 10** The changes of pore deformation pattern for **a** clay, **b** silt, and **c** silty clay soils by depth. Pattern 1: elongated or irregular macropores or coarse mesopores are fractured and transformed into macropores, coarse mesopores, and micropores with relatively small diameters. Pattern 2: compression causes macropores to become coarse mesopores, coarse mesopores to become micropores, and micropores to close



mesopores and micropores became sharper and higher, indicating a higher volume of pores at the corresponding diameter (Fig. 9a, c, e). In this case, pore deformation pattern occurred mostly via transformation of macropores, coarse mesopores collapse into micropores, and partial micropore closure. Combined with parameters such as porosity and pore morphology, the variation in cumulative PSD in these three soil types with depth revealed that the two categories of pore deformation patterns appeared to alternate each other (Fig. 10), except for clay soil. When the pore deformation pattern relied on compression of all pores as depth increased, the closure of micropores tended to reach the limit state. At this point, the pore deformation pattern changed to the collapse of macropores or mesopores, which were irregular or elongated. The redistribution of pores resulted in a different variation of pore numbers and porosity in each pore class and pore morphological categories, and pore orientation became also more random. After redistribution, the compression of all pores became again the driving pore deformation pattern. As expected, the closure limit state of micropores would occur again with increasing depth, and the pore structure would redistribute, too. Such an alternating process tends to be stable as depth increases, and the amount of compression becomes smaller and smaller. This alternate pore deformation pattern was more pronounced in silt and silty clay soils, while its absence in clay soil may be due to sampling depth being lower than for the other two soil types. Xie et al. (2018) also found that pore collapse led to the transformation of large-sized pores into small-sized pores, as well as re-orientation and re-molding of soil pores due to particle rearrangement. However, the evolution of pore structure is related to the change of each pore, which is not easy to measure and requires further study.

## 5 Conclusions

The purpose of the study was to quantify pore characteristics and morphological parameters in three types of soil that mainly lead to land subsidence, and examine the changes as affected by the soil type and the depth of observation using parameters derived from CT-based measurements. We also tried to analyze the correlation between these parameters in the various soil types, discuss the pore size distribution, and determine the pore deformation pattern under a simulated compaction condition. In silt, the number of pores was the smallest but the porosity was large, the proportion of elongated pores was the highest, porosity and macroporosity decreased with depth while coarse mesoporosity, and microporosity increased. In silty clay, porosity and macroporosity decreased with depth, whereas all kinds of pore numbers, coarse mesoporosity, and microporosity increased. The parameters for clay soil did not change significantly. The number of pores was attributed

mainly to micropores, whereas porosity was accounted mainly by macropores. Macropores were mostly elongated, while coarse mesopores were irregular and micropores were regularly shaped. As depth increased, the proportion of elongated pores in silt and silty clay decreased, while SMI and the Euler number increased, which indicates that silt and silty clay are more susceptible to compression and their elongated macropores are more prone to collapse. The alternate pore deformation pattern was also distinct in silt and silty clay soils. In addition, silt and silty clay soils are relatively thick in this area, so the elongated macropores of silt and silty clay soils are the main contributors to land subsidence. The results of the study provide a useful reference for reducing soil compaction in the region and optimizing the groundwater exploitation layer to alleviate land subsidence.

**Acknowledgments** This study was supported by Xi'an Center of Geological Survey Project "1: 50,000 Hydrogeological and Engineering geological survey about major district of Guanzhong Basin" (12120113004800). National Key R&D Program of China (2018YFC0406404), and Program of the China Geological Survey (DD20189270).

## References

- Beven K, Germann P (1982) Macropores and water flow in soils. *Water Resour Res* 18(5):1311–1325
- Bhattacharyya R, Prakash V, Kundu S, Gupta HS (2006) Effect of tillage and crop rotations on pore size distribution and soil hydraulic conductivity in sandy clay loam soil of the Indian Himalayas. *Soil Tillage Res* 86(2):129–140
- Bian X, Cao YP, Wang ZF, Ding GQ, Lei GH (2017) Effect of super-absorbent polymer on the undrained shear behavior of cemented dredged clay with high water content. *J Mater Civ Eng* 29(7): 04017023
- Bian X, Wang ZF, Ding GQ, Cao YP (2016) Compressibility of cemented dredged clay at high water content with super-absorbent polymer. *Eng Geol* 208:198–205
- Cameira MR, Fernando RM, Pereira LS (2003) Soil macropore dynamics affected by tillage and irrigation for a silty loam alluvial soil in southern Portugal. *Soil Tillage Res* 70(2):131–140
- Carlson WD, Rowe T, Ketcham RA, Colbert MW (2003) Applications of high-resolution X-ray computed tomography in petrology, meteoritics and palaeontology. *Geol Soc Lond Spec Publ* 215(1):7–22
- Cássaro FAM, Borkowski AK, Pires LF, Rosa JA, Saab SDC (2011) Characterization of a Brazilian clayey soil submitted to conventional and no-tillage management practices using pore size distribution analysis. *Soil Tillage Res* 111(2):175–179
- Cheng WC, Ni JC, Arulrajah A, Huang HW (2018a) A simple approach for characterising tunnel bore conditions based upon pipe-jacking data. *Tunn Undergr Space Technol* 71:494–504
- Cheng WC, Ni JC, Shen JS, Wang ZF (2018b) Modeling of permeation and fracturing grouting in sand: laboratory investigations. *J Test Eval* 46(5):2067–2082

- Cheng WC, Ni JC, Shen JSL, Huang HW (2017a) Investigation into factors affecting jacking force: a case study. *Proc Inst Civ Eng Geotech Eng* 170(4):322–334
- Cheng WC, Ni JC, Shen SL (2017b) Experimental and analytical modeling of shield segment under cyclic loading. *Int J Geomech* 17(6):04016146
- Cui ZD (2008) Study on the land subsidence caused by the dense high-rise building group in the soft soil area. Dissertation, Tongji University (in Chinese)
- da Costa PA, Mota JCA, Romero RE, Freire AG, Ferreira TO (2014) Changes in soil pore network in response to twenty-three years of irrigation in a tropical semiarid pasture from Northeast Brazil. *Soil Tillage Res* 137:23–32
- Dal Ferro N, Charrier P, Morari F (2013) Dual-scale micro-CT assessment of soil structure in a long-term fertilization experiment. *Geoderma* 204:84–93
- Doube M, Kłosowski MM, Arganda-Carreras I, Cordelières FP, Dougherty RP, Jackson JS, Schmid B, Hutchinson JR, Shefelbine SJ (2010) BoneJ: free and extensible bone image analysis in ImageJ. *Bone* 47(6):1076–1079
- Du YJ, Jiang NJ, Shen SL, Jin F (2012) Experimental investigation of influence of acid rain on leaching and hydraulic characteristics of cement-based solidified/stabilized lead contaminated clay. *J Hazard Mater* 225:195–201
- Feng Y, Wang JM, Liu T, Bai ZK, Reading L (2018) Using computed tomography images to characterize the effects of soil compaction resulting from large machinery on three-dimensional pore characteristics in an opencast coal mine dump. *J Soils Sediments* 2018:1–12
- Gambolati G, Freeze RA (1973) Mathematical simulation of the subsidence of Venice: 1. Theory. *Water Resour Res* 9(3):721–733
- Gambolati G, Gatto P, Freeze RA (1974) Mathematical simulation of the subsidence of Venice: 2. Results. *Water Resour Res* 10(3):563–577
- Gantzer CJ, Anderson SH (2002) Computed tomographic measurement of macroporosity in chisel-disk and no-tillage seedbeds. *Soil Tillage Res* 64(1–2):101–111
- Griffiths FJ, Joshi RC (1991) Change in pore size distribution owing to secondary consolidation of clays. *Can Geotech J* 28(1):20–24
- Gu K, Shi B, Liu C, Jiang HT, Li TB, Wu JH (2018) Investigation of land subsidence with the combination of distributed fiber optics sensing techniques and microstructure analysis of soils. *Eng Geol* 240:34–47
- Gupta SC, Sharma PP, Defranchi SA (1989) Compaction effects on soil structure. *Adv Agron* 42:311–338
- Harrigan TP, Mann RW (1984) Characterization of microstructural anisotropy in orthotropic materials using a 2nd rank tensor. *J Mater Sci* 19(3):761–767
- Hildebrand T, Rügsegger P (1997) Quantification of bone microarchitecture with the structure model index. *Comp Methods Biomechan Biomed Eng* 1(1):15–23
- Hong ZS, Tateishi Y, Han J (2006) Experimental study of macro- and microbehavior of natural diatomite. *J Geotech Geoenviron Eng* 132(5):603–610
- Hu X, Li XY, Guo LL, Liu Y, Wang P, Zhao YD, Cheng YQ, Lyu YL, Liu LY (2018a) Influence of shrub roots on soil macropores using X-ray computed tomography in a shrub-encroached grassland in northern China. *J Soils Sediments* 2018:1–11
- Hu X, Li ZC, Li XY, Liu LY (2016) Quantification of soil macropores under alpine vegetation using computed tomography in the Qinghai Lake watershed, NE Qinghai-Tibet plateau. *Geoderma* 264:244–251
- Hu X, Lyu YL, Liu Y, Li XY, Sun ZT, Li ZC, Cheng YQ, Guo LL, Liu LY (2018b) Enclosure on CT-measured soil macropore characteristics in the Inner Mongolia grassland of northern China. *J Soils Sediments* 18(3):718–726
- Kim H, Anderson SH, Motavalli PP, Gantzer CJ (2010) Compaction effects on soil macropore geometry and related parameters for an arable field. *Geoderma* 160(2):244–251
- Kutflak M (2004) Soil hydraulic properties as related to soil structure. *Soil Tillage Res* 79(2):175–184
- Lai JX, He SY, Qiu JL, Chen JX, Wang LX, Wang K, Wang JB (2017) Characteristics of earthquake disasters and aseismic measures of tunnels in Wenchuan earthquake. *Environ Earth Sci* 76(2):94
- Lai JX, Wang XL, Qiu JL, Zhang GZ, Chen JX, Xie YL, Luo YB (2018) A state-of-the-art review of sustainable energy based freeze proof technology for cold-region tunnels in China. *Renew Sust Energ Rev* 82:3554–3569
- Lebron I, Suarez DL, Schaap MG (2002) Soil pore size and geometry as a result of aggregate size distribution and chemical composition. *Soil Sci* 167(3):165–172
- Li TC, Shao MA, Jia YH (2016) Application of X-ray tomography to quantify macropore characteristics of loess soil under two perennial plants. *Eur J Soil Sci* 67(3):266–275
- Li YL, Yang JC, Hu XM (2000) Origin of ground fissures in the Shanxi graben system, northern China. *Eng Geol* 55(4):267–275
- Lipiec J, Hajnos M, Świeboda R (2012) Estimating effects of compaction on pore size distribution of soil aggregates by mercury porosimeter. *Geoderma* 179–180:20–27
- Lipiec J, Kuś J, Słowińska-Jurkiewicz A, Nosalewicz A (2006) Soil porosity and water infiltration as influenced by tillage methods. *Soil Tillage Res* 89(2):210–220
- Low HE, Phoon KK, Tan TS, Leroueil S (2008) Effect of soil microstructure on the compressibility of natural Singapore marine clay. *Can Geotech J* 45(2):161–176
- Luo LF, Lin H, Li SC (2010) Quantification of 3-D soil macropore networks in different soil types and land uses using computed tomography. *J Hydrol (Amsterdam, Neth)* 393(1–2):53–64
- Ma RM, Cai CF, Li ZX, Wang JG, Xiao TQ, Peng GY, Yang W (2015) Evaluation of soil aggregate microstructure and stability under wetting and drying cycles in two Ultisols using synchrotron-based X-ray micro-computed tomography. *Soil Tillage Res* 149:1–11
- Meng C, Niu JZ, Li X, Luo ZT, Du XQ, Du J, Lin XN, Yu XX (2017) Quantifying soil macropore networks in different forest communities using industrial computed tomography in a mountainous area of North China. *J Soils Sediments* 17(9):2357–2370
- Mooney SJ (2002) Three-dimensional visualization and quantification of soil macroporosity and water flow patterns using computed tomography. *Soil Use Manag* 18(2):142–151
- Mooney SJ, Morris C (2008) A morphological approach to understanding preferential flow using image analysis with dye tracers and X-ray computed tomography. *Catena* 73(2):204–211
- Naveed M, Schjøning P, Keller T et al (2016) Quantifying vertical stress transmission and compaction-induced soil structure using sensor mat and X-ray computed tomography. *Soil Tillage Res* 158:110–122
- Pachepsky Y, Yakovchenko V, Rabenhorst MC, Pooley C, Sikora LJ (1996) Fractal parameters of pore surfaces as derived from micromorphological data: effect of long-term management practices. *Geoderma* 74(3–4):305–319
- Pagliai M, Marsili A, Servadio P, Vignozzi N, Pellegrini S (2003) Changes in some physical properties of a clay soil in Central Italy following the passage of rubber tracked and wheeled tractors of medium power. *Soil Tillage Res* 73:119–129
- Pagliai M, Vignozzi N, Pellegrini S (2004) Soil structure and the effect of management practices. *Soil Tillage Res* 79(2):131–143
- Pöhlitz J, Rücknagel J, Koblenz B, Schlüter S, Vogel HJ, Christen O (2018) Computed tomography and soil physical measurements of compaction behavior under strip tillage, mulch tillage and no tillage. *Soil Tillage Res* 175:205–216
- Powrie W (2014) *Soil mechanics: concepts and applications*. CRC Press, London



- Qiu JL, Wang XL, He SY, Liu HQ, Lai JX, Wang LX (2017) The catastrophic landslide in Maoxian County, Sichuan, SW China, on June 24, 2017. *Nat Hazards* 89(3):1485–1493
- Qiu JL, Wang XL, Lai JX, Zhang Q, Wang JB (2018) Response characteristics and preventions for seismic subsidence of loess in Northwest China. *Nat Hazards* 92(3):1909–1935
- Rabbi SMF, Daniel H, Lockwood PV, Macdonald C, Pereg L, Tighe M, Wilson BR, Young IM (2016) Physical soil architectural traits are functionally linked to carbon decomposition and bacterial diversity. *Sci Rep* 6:33012
- Rachman A, Anderson SH, Gantzer CJ (2005) Computed-tomographic measurement of soil macroporosity parameters as affected by stiff-stemmed grass hedges. *Soil Sci Soc Am J* 69(5):1609–1616
- Reichert JM, Amado TJC, Reinert DJ, Rodrigues MF, Suzuki LEAS (2016) Land use effects on subtropical, sandy soil under sandization/desertification processes. *Agric Ecosyst Environ* 233:370–380
- Schäffer B, Mueller TL, Stauber M, Müller R, Keller M, Schulin R (2008) Soil and macro-pores under uniaxial compression. II Morphometric analysis of macro-pore stability in undisturbed and repacked soil. *Geoderma* 146(1–2):175–182
- Schäffer B, Stauber M, Müller R, Schulin R (2007) Changes in the macro-pore structure of restored soil caused by compaction beneath heavy agricultural machinery: a morphometric study. *Eur J Soil Sci* 58(5):1062–1073
- Shen SL, Wang JP, Wu HN, Xu YS, Ye GL, Yin ZY (2015) Evaluation of hydraulic conductivity for both marine and deltaic deposit based on piezocone test. *Ocean Eng* 110:174–182
- Shen SL, Wang ZF, Cheng WC (2017) Estimation of lateral displacement induced by jet grouting in clayey soils. *Géotechnique* 67(7):621–630
- Terzaghi K (1943) *Theoretical soil mechanics*. Wiley, New York
- Tuller M, Or D, Dudley LM (1999) Adsorption and capillary condensation in porous media: liquid retention and interfacial configurations in angular pores. *Water Resour Res* 35(7):1949–1964
- Udawatta RP, Anderson SH, Gantzer CJ, Garrett HE (2006) Agroforestry and grass buffer influence on macropore characteristics. *Soil Sci Soc Am J* 70(5):1763–1773
- Udawatta RP, Anderson SH, Gantzer CJ, Garrett HE (2008) Influence of prairie restoration on CT-measured soil pore characteristics. *J Environ Qual* 37(1):219–228
- Wang YQ, Wang ZF, Cheng WC (2019) A review on land subsidence caused by groundwater withdrawal in Xi'an, China. *Bull Eng Geol Environ* 78(4):2851–2863
- Wang ZF, Shen JS, Cheng WC (2018) Simple method to predict ground displacements caused by installing horizontal jet-grouting columns. *Math Probl Eng*:1897394
- Wang ZF, Shen SL, Cheng WC, Xu YS (2016) Ground fissures in Xi'an and measures to prevent damage to the metro tunnel system due to geohazards. *Environ Earth Sci* 75(6):511
- Wu JC, Shi XQ, Xue YQ, Zhang Y, Wei ZX, Yu J (2008) The development and control of the land subsidence in the Yangtze Delta, China. *Environ Geol* 55(8):1725–1735
- Xie WL, Li P, Zhang MS, Cheng TE, Wang Y (2018) Collapse behavior and microstructural evolution of loess soils from the loess plateau of China. *J Mt Sci* 15(8):1642–1657
- Xu YS, Shen SL, Cai ZY, Zhou GY (2008) The state of land subsidence and prediction approaches due to groundwater withdrawal in China. *Nat Hazards* 45(1):123–135
- Xue YQ, Zhang Y, Ye SJ, Wu JC, Li QF (2005) Land subsidence in China. *Environ Geol* 48(6):713–720
- Yin YP, Zhang ZC, Zhang KJ (2005) Land subsidence and countermeasures for its prevention in China. *Chin J Geol Hazard Control* 16(2):1–8 (in Chinese)
- Zhao D, Xu MX, Liu GB, Ma LY, Zhang SM, Xiao TQ, Peng GY (2017a) Effect of vegetation type on microstructure of soil aggregates on the loess plateau, China. *Agric Ecosyst Environ* 242:1–8
- Zhao D, Xu MX, Liu GB, Yao X, Tuo DF, Zhang RR, Xiao TQ, Peng GY (2017b) Quantification of soil aggregate microstructure on abandoned cropland during vegetative succession using synchrotron radiation-based micro-computed tomography. *Soil Tillage Res* 165:239–246
- Zhou X, Lin HS, White EA (2008) Surface soil hydraulic properties in four soil series under different land uses and their temporal changes. *Catena* 73(2):180–188

**Publisher's note** Springer Nature remains neutral with regard to jurisdictional claims in published maps and institutional affiliations.